arXiv:1507.02223v1 [cond-mat.quant-gas] 8 Jul 2015

Topological Thouless Pumping of Ultracold Fermions

Shuta Nakajima[1],* Takafumi Tomita[1], Shintaro Taie[1], Tomohiro Ichinose[1], Hideki Ozawa[1], Lei Wang[2], Matthias Troyer[2], and Yoshiro Takahashi[1]
[1] *Department of Physics, Graduate School of Science, Kyoto University, Japan 606-8502*
[2] *Theoretische Physik, ETH Zurich, 8093 Zurich, Switzerland*
(Dated: July 9, 2015)

A gas of electrons in a one-dimensional periodic potential can be transported even in the absence of a voltage bias if the potential is modulated slowly and periodically in time. Remarkably, the transferred charge per cycle is only sensitive to the topology of the path in parameter space. Although this so-called Thouless charge pump has first been proposed more than thirty years ago [1], it has not yet been realized. Here we report the first demonstration of topological Thouless pumping using ultracold atoms in a dynamically controlled optical superlattice. We observe a shift of the atomic cloud as a result of pumping and extract the topological invariance of the pumping process from this shift. We demonstrate the topological nature of the Thouless pump by varying the topology of the pumping path and verify that the topological pump indeed works in the quantum region by varying speed and temperature.

Topology manifests itself in physics in a variety of ways [2–4], with the integer quantum Hall effect (IQHE) being one of the best-known examples in condensed matter systems. There, the Hall conductance of a two-dimensional electron gas is quantized very precisely in units of fundamental constants [5]. As discussed in the celebrated Thouless-Kohmoto-Nightingale-den Nijs paper [4], this quantized value is given by a topological invariant, the sum of the Chern numbers of the occupied energy bands. In 1983, Thouless considered a seemingly different phenomenon of quantum transport of an electron gas in an infinite one-dimensional periodic potential, driven in a periodic cycle [1]. This appears to be similar to the famous Archimedes screw [7], which pumps water via a rotating spiral tube. However, while the Archimedes screw follows classical physics and the pumped amount of water can be continuously changed by tilting the screw, the charge pumped by the Thouless pump is a topological quantum number and not affected by a smooth change of parameters [1]. Interestingly, this quantization of pumped charge shares the same topological origin as the IQHE. The charge pumped per cycle can be expressed by the Chern number defined over a (1+1) dimensional periodic Brillouin zone formed by quasimomentum and time. Although several single electron pumping experiments have been implemented in nanoscale devices such as quantum dots with modulated gate voltages [8–10] or surface acoustic waves in order to create a potential periodic in time [11], the topological Thouless pump with sufficiently long spatial periodicity (which is crucial for achieving topological quantization [1]) has not been realized in electron systems.

In this Letter, we report a realization of Thouless' topological charge pump by exploiting the controllability of ultracold atoms in an optical superlattice. Differently from recent realizations of topological bands in two (spatial or synthetic) dimensions [12–17] our experiment explores the topology of a (1+1) dimensional adiabatic process, in which a dynamically controllable one-dimensional optical superlattice is implemented following the proposal of Ref. [18]. Topological pumping is seen as a shift of the center of mass (CM) of an atomic cloud measured with *in situ* imaging. We extract the Chern number of the pumping procedure from the average shift of the CM per pumping cycle. The topological nature of the pump is revealed by the clear dependence on the topology of the pumping trajectories in parameter space. Our work introduces a new experimental platform to study topological quantum phenomena in adiabatic driven systems.

In our experiments, an ultracold Fermi gas of ytterbium atoms ^{171}Yb is prepared (see Methods A) and loaded into a dynamically controlled optical superlattice. Specifically, we construct a stationary 266nm-spacing optical lattice (short lattice) created by retro-reflection of a 532nm laser beam and a 532nm-spacing optical lattice (long lattice) with a time-dependent phase created by the interference of two 532nm laser beams, which is stabilized by a Michelson interferometer (see Methods B). As a result, these laser beams create the required [18] time-dependent one-dimensional optical superlattice of the form

$$V(z,t) = -V_S(t)\cos^2\left(\frac{2\pi z}{d}\right) - V_L(t)\cos^2\left(\frac{\pi z}{d} - \phi(t)\right), \tag{1}$$

where $d = 532$nm is the lattice constant of the superlattice, V_S is the depth of the short lattice, V_L the depth of the long lattice, and ϕ is the phase difference between the two lattices. In our experiments, V_S and V_L are controlled by the respective laser powers and ϕ by changing the optical path difference between the two interfering beams with a piezo-transducer (PZT)-mounted mirror, which enables us to sweep ϕ up to $\sim 11\pi$ corresponding to more than ten pumping cycles. In the following, we use the lattice constant d as the unit of length and the recoil energy $E_R = h^2/(8md^2)$ as the unit of energy, where

* Electronic address: shuta@scphys.kyoto-u.ac.jp

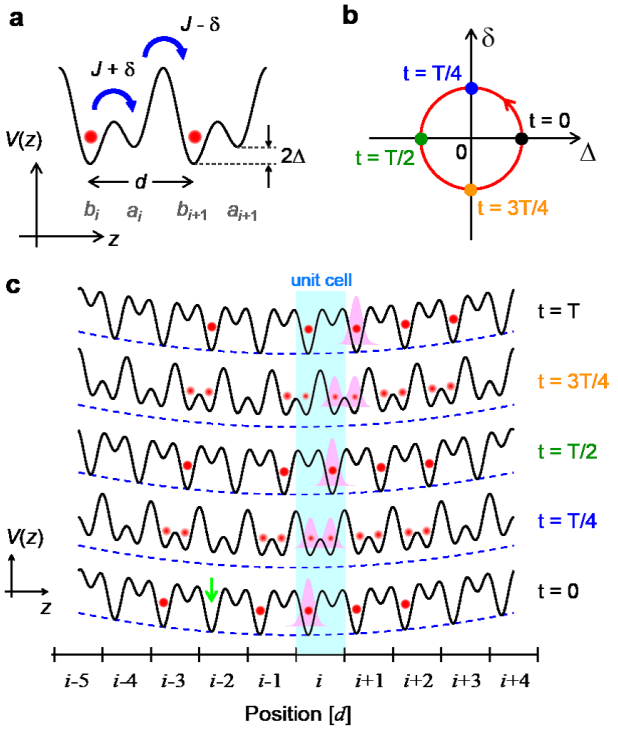

FIG. 1. **The Rice-Mele model. a**. Schematic of the Rice-Mele model. **b**. A pumping cycle sketched (qualitatively) in δ-Δ space. **c**. Schematic of the continuous Rice-Mele (cRM) pumping sequence. The pink shaded packet indicates the wave function of a particular atom initially localized at the unit cell i. The wave function shifts to right as the pumping proceeds and moves the atom to unit cell $i+1$ after one pumping cycle. The blue dashed curve and the green arrow indicate the harmonic confinement (not in scale) and an initial hole, respectively.

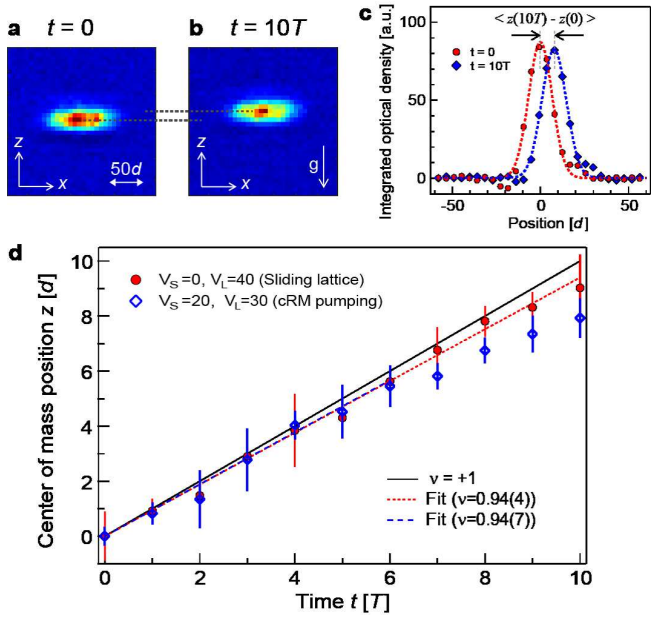

FIG. 2. **Observation of cRM pumping and sliding lattice pumping. a-b**. *In situ* absorption images on the CCD before and after 10 cRM pumpings. **c**. One-dimensional optical densities (integrated along the x axis) before pumping (red circles, same data as **a**) and after 10 cRM pumping (blue diamonds, same data as **b**). **d**. The center of mass (CM) of the atomic cloud after up to ten pumping cycles. Red circles and blue open diamonds indicate the CM shift of the sliding lattice and the cRM pumping lattice, respectively. Error bars denote standard deviation of five independent measurements.

m is the atomic mass of ^{174}Yb (see Methods B).

We load ^{171}Yb atoms into an array of one-dimensional optical superlattices, ensuring that they occupy the lowest energy band (see Supplementary Information S3), and slowly sweep ϕ over time. The lattice potential returns to its initial configuration whenever ϕ changes by π, thus completing a pumping cycle. Since the lattice potential is periodic both in space and time, one can define energy bands and corresponding topological invariants such as the Chern number in a k-t Brillouin zone, where k is the quasimomentum and t is the time. We have ensured that the band gap never closes during the whole pumping procedure so ideally the atoms stay in the lowest band during the adiabatic pumping process. The phase sweep breaks time-reversal symmetry and the energy bands can acquire a non-zero Chern number. According to [1], the number of atoms transferred in one cycle is then proportional to the Chern number of the occupied band.

The ability to tune all parameters of the lattice potential (1) independently in a dynamic way offers the opportunity to realize various pumping protocols. In the absence of the static short lattice, $V(z,t)$ describes a simple sliding lattice which Thouless originally proposed [1]. Including the V_S term, one realizes a double-well lattice illustrated in Fig. 1. A pictorial understanding of this alternative pumping process is provided by the tight-binding Rice-Mele model [6, 20],

$$\hat{\mathcal{H}} = \sum_i \left(-(J+\delta)\hat{a}_i^\dagger \hat{b}_i - (J-\delta)\hat{a}_i^\dagger \hat{b}_{i+1} + \text{h.c.} + \Delta(\hat{a}_i^\dagger \hat{a}_i - \hat{b}_i^\dagger \hat{b}_i) \right), \tag{2}$$

where $\hat{a}_i$ and $\hat{b}_i$ are fermionic annihilation operators in the two sublattices of the i-th unit cell, $J \pm \delta$ is the tunnelling amplitude within and between unit cells, and Δ denotes a staggered on-site energy offset, as shown in Fig. 1a. We ignore the spin degree of freedom since we can neglect the interaction between the two spin components due to a very small s-wave scattering length [21].

Figure 1c shows the schematics of our "continuous Rice-Mele" (cRM) pumping sequence. Sweeping the phase linearly in time as $\phi(t) = \pi t/T$ the hopping amplitudes and on-site energies are modulated periodically. Our *ab initio* calculation shows that the cRM pumping scheme used in the experiment is topologically equivalent to the Rice-Mele model for atoms that reside in the lowest energy band since the Chern numbers are the same (see Supplementary Information S2). In the following, we will thus use the tight-binding Rice-Mele Hamiltonian to sim-

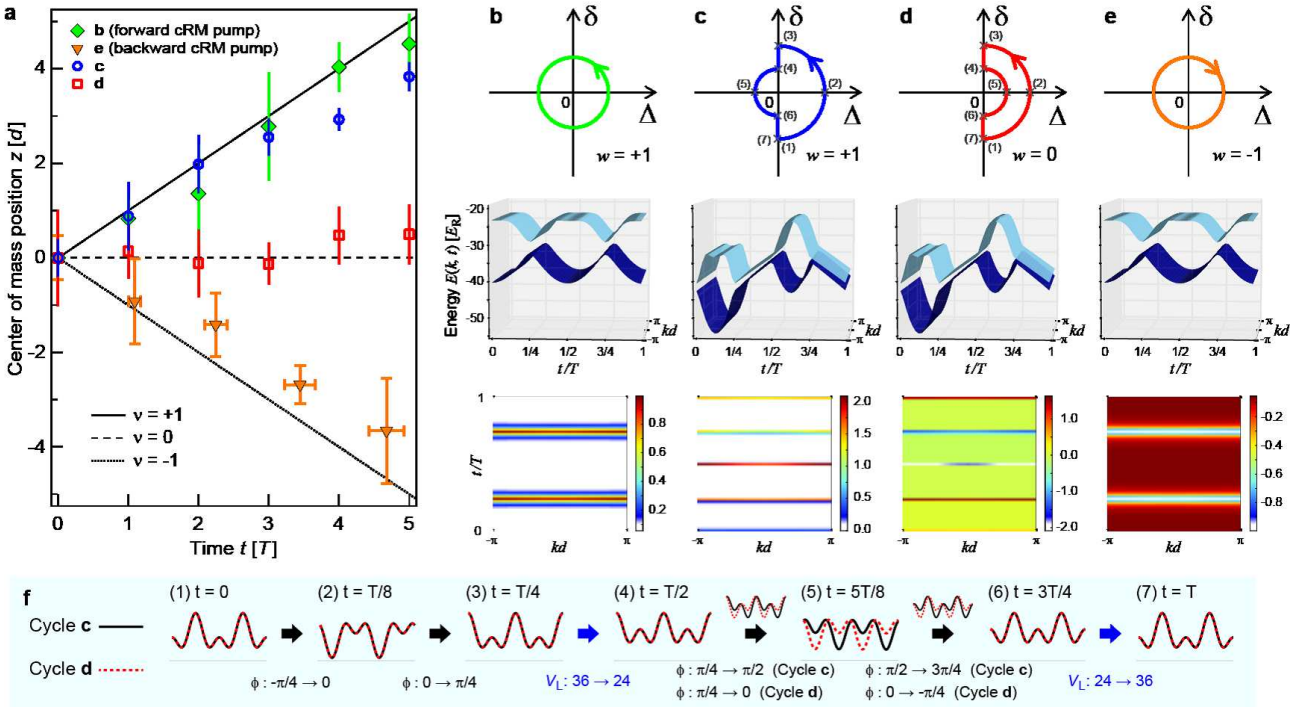

FIG. 3. **Topological aspects of cRM pumping**. **a**. Charge pumped during a simple cRM pumping (**b**), topologically-nontrivial pumping (**c**) topologically-trivial pumping (**d**), and negative sweep cRM pumping (**e**). The vertical error bars denote the standard deviation of three to five independent measurements and the horizontal error bar for the negative sweep data indicates a possible shift due to the nonlinearity and hysteresis of the PZT for negative sweep direction. **b-e**. Pumping sequences in the δ-Δ plane (top), the corresponding band structures in the k-t Brillouin zone (middle), and the Berry curvatures of the pumping cycles (bottom). The indices w in the top figures indicate the winding number of each trajectory around the origin. **f**. Schematic pumping sequences of the cycles **c** and **d**. The phase ϕ and the depth V_L of the long lattice are linearly swept alternatingly. The short lattice depth V_S is fixed to 30 E_R and the pumping period T is 100 ms for both cycles.

plify the discussion of the pumping sequence as a closed trajectory in the δ-Δ parameter plane (Fig. 1b).

Figure 2 shows the main results of our pumping experiments. Our stable absorption imaging system with a charge-coupled-device (CCD) camera enables us to accurately measure the shift of the CM of the atomic cloud after several pumping cycles (see Supplementary Information S4), as shown in Figs. 2a and b. The period T is fixed to 50 ms for the results shown in Fig. 2. One can clearly recognize the sizable CM shift along the z-direction. We plot the *in situ* CM positions of the atomic cloud after a few pumping cycles in Fig. 2d. The averaged CM shift per cycle $\langle z(t) - z(0) \rangle / (td)$ of the cRM pumping with $(V_S, V_L) = (20, 30)E_R$ is evaluated to be 0.94(7) for $t \leq 6T$. This provides a direct measurement of the Chern number of the occupied energy band, which is consistent with the ideal value $\nu = 1$. As a comparison, the observed average CM shift per cycle of a sliding lattice $(V_S, V_L) = (0, 40)E_R$ is 0.94(4), which is again close to the ideal value of $\nu = 1$. Classically it is quite intuitive that the sliding lattice is able to transfer atoms because the potential minima are moving in space. However, even though the potential minima of the cRM pump $(V_S, V_L) = (20, 30)E_R$ are not moving in space as shown in Fig. 1c, the pumping is topologically equivalent because of the same Chern number of the occupied band. The cRM lattice has the same ability to transfer atoms residing in the lowest energy band, even though the pumping is achieved by a sequence of quantum tunneling events between the double-wells (see Supplementary Information S3). We attribute the saturating behavior of the cRM pumping for $t > 6T$ to the effect of the harmonic confinement, whose variation can be comparable to the band gap for large CM shift [22] (see Supplementary Information S5).

A striking feature of our pump is its *topological* nature. In particular, the pumped amount in the Rice-Mele model [7, 24] is directly related to the topology of the trajectory in the δ-Δ plane. It *only* depends solely on the winding number w of the trajectory that encloses the origin $\delta = \Delta = 0$ (see Supplementary Information S2). Note that electron pumping in restricted nano-devices [8–11] is not topological since there the amount of the charge pumped per cycle instead depends on the area of the enclosed parameter space [25], which is the geometry but not the topology of the trajectory. To highlight the topological nature of Rice-Mele pumping, we investigate four distinct pumping sequences with trajectories shown schematically in Figs. 3b-e. In Fig. 3a, we plot the CM shifts of two cRM pumping schemes with

$(V_S, V_L) = (20, 30)E_R$ (Fig. 3b,e) and two amplitude-modified cRM pumping schemes (Fig. 3c, d). Evidently, the sequence which does not wind around the origin (Fig. 3d) results in no pumping, and those with winding trajectories (Fig. 3b,c and e) result in finite pumping. This is direct evidence of the topological nature of the pump. Note that the band structure in the k-t space of the non-trivial pumping sequence (Fig. 3c) is *identical* to that of the trivial pumping (Fig. 3d). However, the Berry curvature and the Chern number of the lowest band are different. This highlights the fact that the pumped charge is a topological quantity, which depends on the wave function but not on the band dispersions. Furthermore, we also performed the cRM pumping with a negative sweep of the phase $\phi(t) = -\pi t/T$, which corresponds to an opposite winding in δ-Δ plane and the cloud is pumped to the opposite direction even though the band dispersion remains identical to that of the forward sweep pumping (Fig. 3e).

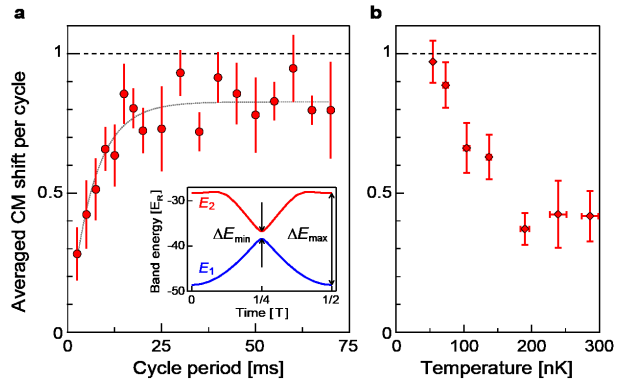

FIG. 4. **Conditions for quantum pumping.** The averaged CM shift per cycle after five cycles. **a**. Sweep speed dependence of the cRM pumping. The horizontal axis corresponds to the period T of one pumping cycle. The inset shows instantaneous band maxima E_1 of the first band and minima E_2 of the second band for $(V_S, V_L) = (30, 30)E_R$. The pumped amount saturates as the pumping speed slows down. The dotted curve shows an exponential fit with time constant (6.5 ± 1.2) ms. The error bars denote standard deviation of three independent measurements. **b**. Finite temperature effect in the cRM pumping. The pumped amount approaches the ideal value as the temperature decreases The error bars denote the standard deviation of five independent measurements and the horizontal error bar indicates standard deviation of five temperature measurements before the lattice loading.

A crucial requirement of the topological Thouless pump is adiabaticity, requiring that the band gap never closes during the pumping process and that the atoms always remain in the lowest energy band. Figure 4a shows the pumping period dependence of the cRM pumping with the depths of $(V_S, V_L) = (30, 30)E_R$. The data suggest that a pumping time of $T \gtrsim 30$ms is long enough to achieve a saturated pumped charge in this lattice potential. This can be understood from considering Landau-Zener transitions to the higher band. The instantaneous energy gap $\Delta E(t) = E_2 - E_1$ changes in time as shown in the inset of Fig. 4a. The probability of diabatic transitions is given by the Landau-Zener formula $P = e^{-2\pi\Gamma}$, where $\Gamma = (\Delta E_{\rm min}/2)^2/\hbar\frac{d}{dt}(\Delta E(t))$. In our case, $\Delta E_{\rm min} = 1.6E_R$ and $\Delta E_{\rm max} = 20E_R$. Since the energy sweep speed is on the order of $8\Delta E_{\rm max}/T$, we find that $2\pi\Gamma \sim T/(6\text{ ms})$, which is consistent with the observed result.

We next check the temperature dependence of our pump. Figure 4b shows the pumped amount as a function of the temperature of the gas before loading into the lattice of the depths $(V_S, V_L) = (25, 30)E_R$. The temperature is tuned by changing the sympathetic evaporative cooling condition while keeping the same number of ^{171}Yb atoms. One can see that pumping reaches the ideal value at the lowest temperature of 54(1)nK. While the temperature given in Fig. 4b is not the temperature in the lattice but that before lattice loading, the observed temperature dependence exhibits similar behavior to that discussed in Ref. [18]: pumping efficiency reaches its ideal value once the temperature is lower than the gap energy.

Having demonstrated topological Thouless pumping using flexible optical superlattice setup, the scheme can be extended to even more novel setups. For example, by choosing a special lattice laser frequency, one can create a spin dependent superlattice [26] which realizes Z_2-spin pumping [27], a counterpart of Z_2 topological insulators. Another possibility is to change the ratio of the long lattice and short lattice wavelengths by tuning the angle of the interferometric lattice, which realizes a superlattice with incommensurate ratios and the Aubry-André model [28] with fractional pumping [29] and anomalous pumping [30]. Furthermore, introducing interaction effect is feasible and will open a door for experimental exploration of the interplay of topological quantum phenomena and interaction and correlation effects.

Note added. Recently, we became aware of similar work carried out by Lohse *et al.* [33] observing the topological Thouless pumping with bosonic atoms in Mott insulator state.

I. METHODS

A. A. Preparation of a degenerate Fermi gas of ^{171}Yb

Since ^{171}Yb atoms have a very short s-wave scattering length of -0.15nm [21], we use sympathetic evaporative cooling with ^{173}Yb atoms to obtain the degenerate Fermi gas of ^{171}Yb [31]. After collecting Yb atoms in a magneto-optical trap using the intercombination transition (556nm), the two isotopes are loaded into a crossed far-off-resonant trap (FORT) with 532nm light. Sympathetic evaporative cooling is performed by continuously decreasing the FORT trap depth. After blowing away the ^{173}Yb atoms by using a 556nm laser which is res-

onant only for ^{173}Yb, we obtain a pure degenerate gas of ^{171}Yb atoms with two hyperfine spin components of $|F = 1/2, m_F = \pm 1/2\rangle$ and a typical number of atoms of 1×10^4 for each spin. The initial temperature before lattice loading can be as low as 60 nK, which is ~ 50 % of the Fermi temperature T_F in the FORT. The trap frequencies of the FORT at the end of the evaporation are $(\omega'_x, \omega'_y, \omega_z)/2\pi = (145, 20, 161)$, where the x'- and y'-axes are tilted from the lattice axes (x and y) by 45°.

B. B. Setup for the optical superlattice

Our one-dimensional optical superlattice setup is a part of our optical Lieb lattice system [8]. To stabilize the phase ϕ of the interfering 532nm-spacing optical lattice (long lattice) we construct a Michelson interferometer with frequency stabilized 507nm laser, whose optical paths are overlapped with the interfering lattice beams until separated from the lattice beams with dichroic mirrors before entering the experimental chamber. The 507nm laser beams are retro-reflected to form the interferometer just after the separation. We can control the phase ϕ by tuning the PZT of the retro-reflection mirror of the z-axis 507nm laser, keeping stabilization of the optical path lengths of the lattice and 507nm beams via another PZT-mounted mirror in the common path as long as the phase sweep speed is smaller than 0.5π rad/ms. The short-term stability of the phase ϕ is estimated to be 0.007π. A phase drift of typically 0.05π per hour, is not a problem since the pumping only depends on the phase difference before and after pumping. The nonlinearity of the PZT and the relative phase ϕ between the long lattice and the short lattice are calibrated via the matter wave interference pattern of a Bose-Einstein condensate (BEC) of ^{174}Yb atoms released from the superlattice. The depths of optical lattices are also calibrated via pulsed lattice with the BEC of ^{174}Yb.

C. C. Calculations of the band structure and Chern number

To predict the pumped charge of the experimental pumping protocols, we calculate the band structures and the Chern numbers of the one-dimensional Hamiltonian $H(z,t) = -\frac{\hbar^2\nabla^2}{2m} + V(z,t)$. The band structure is obtained by solving $H(z,t)\,|\psi_k(t)\rangle = E(k,t)\,|\psi_k(t)\rangle$ in a plane wave basis. The Chern number is then calculated as

$$\nu = \frac{1}{2\pi}\int_0^T dt \int_0^{2\pi/d} dk\,\Omega(k,t), \tag{3}$$

where $\Omega(k,t) = \partial_t A_k - \partial_k A_t$ is the Berry curvature and $A_{t(k)} = i\,\langle u_k(t)|\partial_{t(k)}|u_k(t)\rangle$ is the Berry connection calculated using the periodic part of the Bloch wavefunction $|u_k(t)\rangle = e^{-ikz}\,|\psi_k(t)\rangle$.

ACKNOWLEDGEMENTS

We thank N. Kawakami, S. Fujimoto, J. Ozaki, T. Fukui, I. Maruyama, Y. Hatsugai, and S. Nakamura for valuable discussions and A. Sawada for experimental assistance. This work was supported by the Grant-in-Aid for Scientific Research of JSPS (No. 25220711, No. 24-1698), and the Impulsing Paradigm Change through Disruptive Technologies (ImPACT) program. L.W. and M.T. were supported by ERC Advanced Grant SIMCOFE and by the Swiss National Science Foundation through the National Center of Competence in Research Quantum Science and Technology QSIT. L.W. and M.T. acknowledge Xi Dai for collaborations on the related topic.

AUTHOR CONTRIBUTIONS

S. N. and T. T. carried out experiments and the data analysis. S. T. conceived the experimental techniques for the superlattice. T. I. and H. O. contributed to building up the superlattice setup. L. W. carried out the theoretical calculation. Y. T. conducted the whole experiment. All the authors contributed to the writing of the manuscript.

COMPETING FINANCIAL INTERESTS

The authors declare no competing financial interests.

[1] Thouless, D. J. Quantization of particle transport. *Phys. Rev. B* **27**, 6083–6087 (1983).
[2] Mermin, N. D. The topological theory of defects in ordered media. *Rev. Mod. Phys.* **51**, 591–648 (1979).
[3] Thouless, D. J. *Topological quantum numbers in nonrelativistic physics* (World Scientific Singapore, 1998).
[4] Hasan, M. Z. & Kane, C. L. *Colloquium* : Topological insulators. *Rev. Mod. Phys.* **82**, 3045–3067 (2010).

[5] Klitzing, K. v., Dorda, G. & Pepper, M. New method for high-accuracy determination of the fine-structure constant based on quantized Hall resistance. *Phys. Rev. Lett.* **45**, 494–497 (1980).

[6] Thouless, D. J., Kohmoto, M., Nightingale, M. P. & den Nijs, M. Quantized Hall conductance in a two-dimensional periodic potential. *Phys. Rev. Lett.* **49**, 405–408 (1982).

[7] Altshuler, B. L. & Glazman, L. I. Pumping electrons. *Science* **283**, 1864–1865 (1999).

[8] Switkes, M., Marcus, C. M., Campman, K. & Gossard, A. C. An adiabatic quantum electron pump. *Science* **283**, 1905–1908 (1999).

[9] Blumenthal, M. D. *et al.* Gigahertz quantized charge pumping. *Nature Phys.* **3**, 343–347 (2007).

[10] Kaestner, B. *et al.* Single-parameter nonadiabatic quantized charge pumping. *Phys. Rev. B* **77**, 153301 (2008).

[11] Shilton, J. M. *et al.* High-frequency single-electron transport in a quasi-one-dimensional GaAs channel induced by surface acoustic waves. *J. Phys. Condens. Matter* **8**, L531–L539 (1996).

[12] Aidelsburger, M. *et al.* Realization of the Hofstadter Hamiltonian with ultracold atoms in optical lattices. *Phys. Rev. Lett.* **111**, 185301 (2013).

[13] Miyake, H., Siviloglou, G. A., Kennedy, C. J., Burton, W. C. & Ketterle, W. Realizing the Harper Hamiltonian with laser-assisted tunneling in optical lattices. *Phys. Rev. Lett.* **111**, 185302 (2013).

[14] Jotzu, G. *et al.* Experimental realization of the topological Haldane model with ultracold fermions. *Nature* **515**, 237–240 (2014).

[15] Aidelsburger, M. *et al.* Measuring the Chern number of Hofstadter bands with ultracold bosonic atoms. *Nature Phys.* **11**, 162–166 (2015).

[16] Mancini, M. *et al.* Observation of chiral edge states with neutral fermions in synthetic Hall ribbons. Preprint at http://arXiv.org/abs/1502.02495 (2015).

[17] Stuhl, B. K., Lu, H. I., Aycock, L. M., Genkina, D. & Spielman, I. B. Visualizing edge states with an atomic Bose gas in the quantum Hall regime. Preprint at http://arXiv.org/abs/1502.02496 (2015).

[18] Wang, L., Troyer, M. & Dai, X. Topological charge pumping in a one-dimensional optical lattice. *Phys. Rev. Lett.* **111**, 026802 (2013).

[19] Rice, M. J. & Mele, E. J. Elementary excitations of a linearly conjugated diatomic polymer. *Phys. Rev. Lett.* **49**, 1455–1459 (1982).

[20] Atala, M. *et al.* Direct measurement of the Zak phase in topological Bloch bands. *Nature Phys.* **9**, 795–800 (2013).

[21] Kitagawa, M. *et al.* Two-color photoassociation spectroscopy of ytterbium atoms and the precise determinations of s-wave scattering lengths. *Phys. Rev. A* **77**, 012719 (2008).

[22] Qian, Y., Gong, M. & Zhang, C. Quantum transport of bosonic cold atoms in double-well optical lattices. *Phys. Rev. A* **84**, 013608 (2011).

[23] Xiao, D., Chang, M.-C. & Niu, Q. Berry phase effects on electronic properties. *Rev. Mod. Phys.* **82**, 1959–2007 (2010).

[24] Shen, S.-Q. *Topological insulators: Dirac equation in condensed matters*, vol. 174 (Springer, 2013).

[25] Brouwer, P. W. Scattering approach to parametric pumping. *Phys. Rev. B* **58**, R10135–R10138 (1998).

[26] Mandel, O. *et al.* Coherent transport of neutral atoms in spin-dependent optical lattice potentials. *Phys. Rev. Lett.* **91**, 010407 (2003).

[27] Fu, L. & Kane, C. L. Time reversal polarization and a Z_2 adiabatic spin pump. *Phys. Rev. B* **74**, 195312 (2006).

[28] Aubry, S. & Andre, G. Analyticity breaking and Anderson localization in incommensurate lattices. *Ann. Israel Phys. Soc* **3**, 18 (1980).

[29] Marra, P., Citro, R. & Ortix, C. Fractional quantization of the topological charge pumping in a one-dimensional superlattice. *Phys. Rev. B* **91**, 125411 (2015).

[30] Wei, R. & Mueller, E. J. Anomalous charge pumping in a one-dimensional optical superlattice. Preprint at http://arXiv.org/abs/1502.04208 (2015).

[31] Taie, S. *et al.* Realization of a SU(2) $\times$ SU(6) system of fermions in a cold atomic gas. *Phys. Rev. Lett.* **105**, 190401 (2010).

[32] Taie, S. *et al.* Matter-wave localization and delocalization of ultracold bosons in an optical Lieb lattice. Preprint at http://arXiv.org/abs/1506.00587 (2015).

[33] Lohse, M., Schweizer, C., Zilberberg, O., Aidelsburger, M. & Bloch, I. to be published.

Supplementary Information

S1. POLARIZATION AND PUMPING IN A 1D SYSTEM

Thouless [1] calculated the current in a one-dimensional periodic potential using the Bloch wave function and derived the formula for the quantized particle transport. Here we summarize the derivation of the same formula as the shift of a Wannier functions [2], which is more intuitive and relevant for the experimental realization of a finite and trapped system.

Figure S1 shows the schematics of our pump. We focus on a lattice site at $z = R$. Using the full Bloch function of the lowest band $|\psi_k\rangle = e^{ikz}|u_k\rangle$, the Wannier function of the lowest band localized at the unit cell R is given by

$$|R\rangle = \frac{1}{\sqrt{N}}\sum_{k=-\pi/d}^{\pi/d} e^{-ikR}|\psi_k\rangle = \sqrt{\frac{d}{L}}\sum_{k=-\pi/d}^{\pi/d} e^{ik(z-R)}|u_k\rangle, \tag{4}$$

where $N = L/d$ is the number of unit cells in the system, L the system length and d the lattice constant. The expected shift of the Wannier center from the lattice site R, or "polarization" [2] P at time t can be written as

$$\begin{aligned} P(t) &= \langle R(t)|z-R|R(t)\rangle = \frac{d}{L}\sum_{-\pi/d}^{\pi/d}\langle u_k(t)|\, i\partial_k\,|u_k(t)\rangle \\ &= d\int_{-\pi/d}^{\pi/d}\frac{dk}{2\pi}A_k(k,t). \end{aligned} \tag{5}$$

Here we used the relation $\partial_k|R\rangle = 0$. The quantity $A_k(k,t) = i\langle u_k(t)|\,\partial_k\,|u_k(t)\rangle$ is called the Berry connection and the integration on the right hand side of Eq. (5) is known as the Zak phase [3]. Thus, the spatial shift of the Wannier function from $t = t_1$ to $t = t_2$ or the change of the polarization is given by

$$\Delta P = P(t_2) - P(t_1) = d\int_{-\pi/d}^{\pi/d}\frac{dk}{2\pi}\left[A_k(k,t_2) - A_k(k,t_1)\right] \tag{6}$$

Using Stokes's formula, this can be written as

$$\Delta P = -d\int_{-\pi/d}^{\pi/d}\frac{dk}{2\pi}\int_{t_1}^{t_2} dt\left(\partial_k A_t(k,t) - \partial_t A_k(k,t)\right) \tag{7}$$

where $A_t(k,t) = i\langle u_k(t)|\,\partial_t\,|u_k(t)\rangle$. Then the shift of the Wannier function after one pumping cycle is

$$\Delta P = d\frac{i}{2\pi}\int_0^T dt\int_{-\pi/d}^{\pi/d} dk\left[\left\langle\frac{\partial u_k}{\partial t}\middle|\frac{\partial u_k}{\partial k}\right\rangle - \left\langle\frac{\partial u_k}{\partial k}\middle|\frac{\partial u_k}{\partial t}\right\rangle\right], \tag{8}$$

where $|\frac{\partial u_k}{\partial k}\rangle = \partial_k|u_k\rangle$. This formula is essentially the same as the one derived by Thouless [1]. Such an integral over two parameters in which the Hamiltonian is periodic should give an integer multiple of $2\pi i$, as discussed in TKNN's paper [4]. Therefore, the shift of the cloud after one pumping cycle is simply given as $\Delta P = \nu d$, where ν is the first Chern number. In other words, the shift per cycle divided by d gives the Chern number.

In the above derivation, we assume that the localized function can be written in the Wannier function consisting of the lowest band Bloch function. In the interacting case, a filled band is required for well-defined Wannier functions. However, in our experiments, we can ignore interactions and even if we have thermal excitations (*i.e.* holes), at the beginning of the pumping, each Wannier functions move independently and the center of mass of the cloud is robustly pumped as we observed.

S2. TOPOLOGICAL EQUIVALENCE OF THE PUMPING PROTOCOLS

The simple sliding potential has Chern number $\nu = 1$ for each energy band, therefore the pumped amount is proportional to the band occupation. This is a manifestation of the Galilean invariance of the lattice [5]. By linearly tuning the lattice depth from $(V_S, V_L) = (0, 40)E_R$ to the cRM pumping $(V_S, V_L) = (20, 30)E_R$ with an interpolation parameter $\alpha \in [0, 1]$, the lowest two bands are adiabatically connected without gap closing as shown in Fig. S2a. The lowest two energy bands of the cRM pumping therefore also have Chern number $\nu = 1$. However, a gap closes between the higher bands, and the third band of $(V_S, V_L) = (20, 30)E_R$ lattice has Chern number $\nu = -1$. The above discussion also shows that the topological equivalence of the cRM pumping adopted in the experiment and the two-band tight-binding Rice-Mele model [6] only holds for the lowest band, since the second energy band of the tight binding Rice-Mele model has Chern number $\nu = -1$.

For the Rice-Mele model, the pumping cycle defines a mapping from time to a closed path on the $\Delta - \delta$ plane. Focussing on the lowest energy band, we now show that the pumped amount is related to the winding number of the path in the $\Delta - \delta$ plane [7]. In the periodic gauge the first term in Eq. (S7) vanishes, therefore the change of the polarization is given by the path integral over the Zak phase, which is a smooth function except on the branch cut with a discontinuity of the size one. Figure S2b clearly shows that the resulting change of the polarization will be finite only for paths that wind around $\Delta = \delta = 0$.

In the experimental setup, especially if V_L is comparable or larger than V_S, the modulated tunneling amplitude $J \pm \delta$ changes drastically in the pumping sequence and J is not constant as in the Rice-Mele model. Moreover, hoppings beyond nearest-neighbors may be required to fully capture the band structures. However, these effects do not close the gap and thus do not change the topology of pumping sequence – a manifestation of the topological robustness of this system. Therefore, we can still characterize the pumping using δ and Δ of the Rice-Mele model

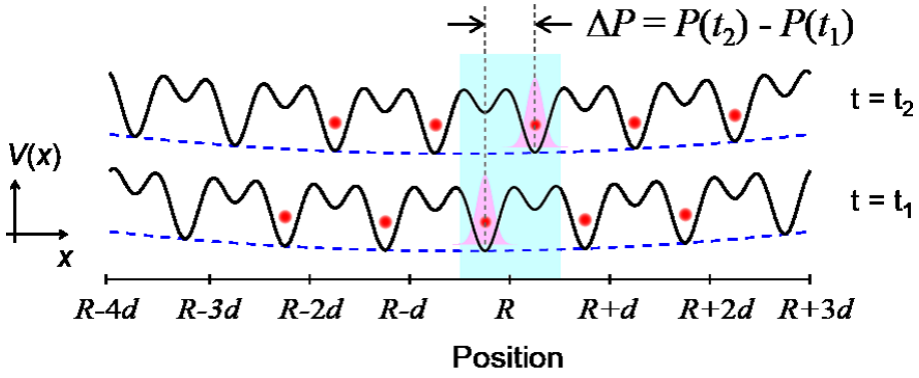

FIG. S 1. **Thouless pumping as a change of the polarization.**

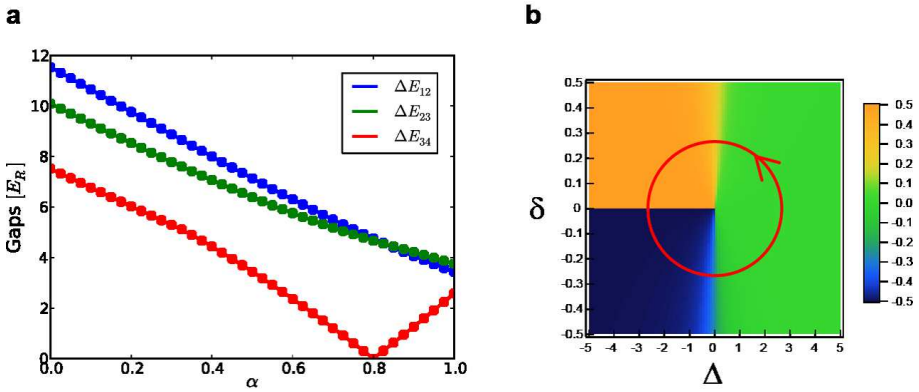

FIG. S 2. **Band gaps and Zak phases.** **a** Band gaps of the interpolated pumping between $(V_S, V_L) = (0, 40)E_R$ and $(20, 30)E_R$. ΔE_{ij} denotes the band gap between energy bands E_i and E_j. **b** Zak phase divided by 2π in the plane of Δ and δ in the Rice-Mele model. The line of discontinuity can be chosen anywhere depending on the gauge phase choice of the eigenstate. The Zak phase or the polarization changes significantly when Δ changes the sign (See also discussion in S3).

even in the experimental situations.

S3. DETAILS OF DYNAMICALLY-CONTROLLED SUPERLATTICE SETUP

In this section we explain the details of our dynamically-controlled optical superlattice setup and discuss the band filling. The lattice laser configuration in the z-x plane is shown in Fig. S3a. The short lattice (a 266nm-spacing optical lattice) in the z-direction is created by retro-reflection of a 532nm laser (green arrow). The long lattice (a 532nm-spacing optical lattice with a time-dependent phase) is created by the interference of two 532 nm laser beams (yellow arrows), stabilized by a Michelson interferometer. As shown in Fig. S3a, the direction of the wavevector of this interferometric lattice or a "diagonal lattice" is not z-axis but $(\hat{\boldsymbol{z}} - \hat{\boldsymbol{x}})$ axis and the lattice has the lattice constant of $d/\sqrt{2} = 376$ nm. Moreover, the phase of the diagonal lattice moves to $(\hat{\boldsymbol{z}} - \hat{\boldsymbol{x}})$ direction as we sweep the PZT in the Michelson interferometer. However, thanks to the x-direction confinement lattice V^x_{1064} created by a standing wave of a 1064 nm laser beam indicated by the red arrow in Fig. S3a, the hopping for the x-direction is suppressed and we can regard the z-direction projected component of this moving diagonal lattice as a moving long lattice along the z-direction, which creates a one-dimensional superlattice potential for the z-direction (S3b).

The setup contains another 532 nm laser to suppress the hopping for the y-direction ($V^y_\perp$) and realize an array of one-dimensional superlattice tubes (Fig. S3(c)). The depth of these vertical confinement lattices are $V^x_{1064} = 35E_R$ and $V^y_\perp = 140E_R$. Since we acquire a y-axis integrated absorption image, we do not observe any difference in pumping even if we lower $V^y_\perp$ so that the tunnelling time along the y-direction is comparable to the pumping period.

We also confirm the absence of the shift of the cloud along the direction perpendicular to the pumping direction. For this purpose, we perform pumping experiments along the z-axis and the x-axis. In Fig. S4 we plot the CM position along the pumping direction (z-axis for **a** and x-axis for **b**) and the perpendicular direction (x-axis for **a** and z-axis for **b**) for both superlattice configura-

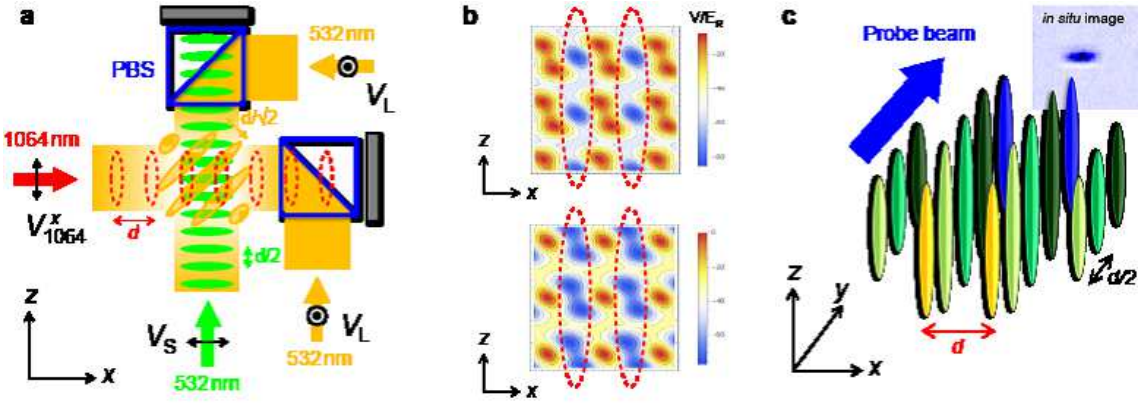

FIG. S 3. **Configuration of our superlattice setup.a**. Laser configuration for the experimental realization of a one-dimensional optical superlattice. Black arrows indicate polarizations of the lattice beams. **b**. Lattice potential for $(V_S, V_L, V^x_{1064}) = (20, 30, 35)$ at $\phi = 0$ (upper) and $\pi/2$ (lower). The red dashed ovals indicate one-dimensional superlattice regions. **c**. Schematic view of our superlattice tubes array and the imaging axis.

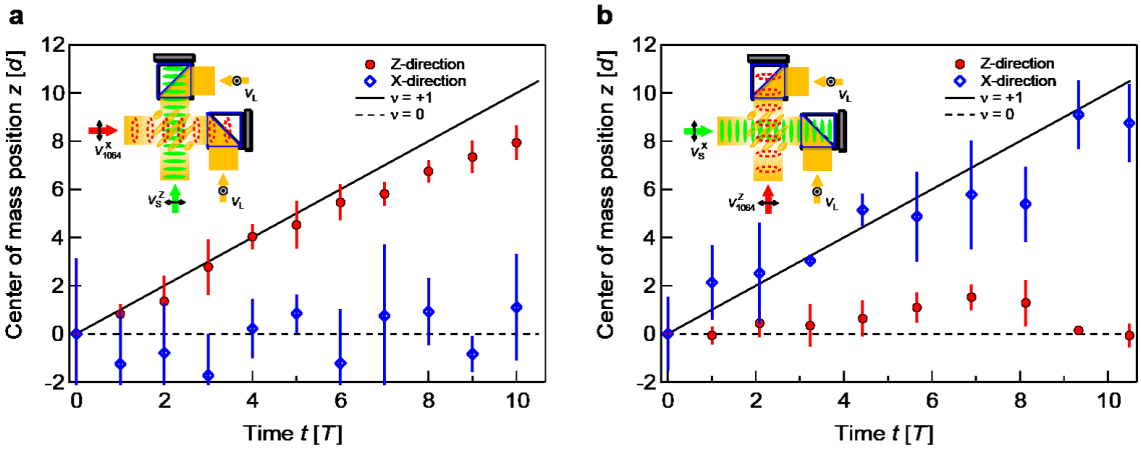

FIG. S 4. **Absence of the shift of the cloud along the perpendicular direction.** **a** The CM shift of the cRM pumping along the pumping direction (z, red circles) and the perpendicular direction (x, blue open diamonds) in the z-axis superlattice configuration (inset of **a**). **b** The CM shift of the cRM pumping along the pumping direction (x, blue open diamonds) and the perpendicular direction (z, red circles) in the x-axis superlattice configuration (inset of **b**). The lattice depths are $(V_S, V_L) = (20, 30)E_R$ for both **a** and **b**.

tions (see insets in Figs. S4a and b). As one can see, there is no spatial shift along the perpendicular directions, which is consistent with our system being an array of one-dimensional superlattices.

To ensure that most of the atoms are loaded into the lowest band of the superlattice, we first ramp up the long lattice potential in 400 ms, whose band gap is much larger than that of the superlattice. We then ramp up the additional short lattice potential in 150 ms. The observed that at least 80 % of the atoms are mapped to the 1st Brillouin zone in our band mapping measurements. Considering the non-adiabatic transition to the higher band during the band mapping, the actual occupation of the lowest band should be larger than this observed value.

Moreover, we also confirmed that the atoms are always in the lowest band of the superlattice during one pumping sequence by using the "sublattice mapping technique" developed in our recent Lieb lattice experiment [8]. In this method, we first quickly change the lattice potential to a "mapping lattice" with $(V_S, V^z_{1064}) = (40, 10)E_R$ and a fixed relative phase $\phi = 0$ in 0.3 ms right after the pumping sequence. In this mapping lattice configuration, the A-sublattice $\{a_i\}$ is energetically well separated from the B-sublattice $\{b_i\}$ and the lowest two bands consist of the A- and B-sublattices, respectively. This maps sublattice occupations after the pumping sequence to band occupations, which then can be measured by band mapping techniques. Figure S5a, b and c show a schematic description of our sublattice mapping technique. In Fig. S5d, we show the sublattice mapping measurements for a cRM pumping sequence with the potential depths of $(V_S, V_L) = (20, 26)E_R$. As one can see in Fig. S5d, the band mapping result at $t = 0$, $t = T$ and $t = 2T$ are almost the same, namely the atoms in the

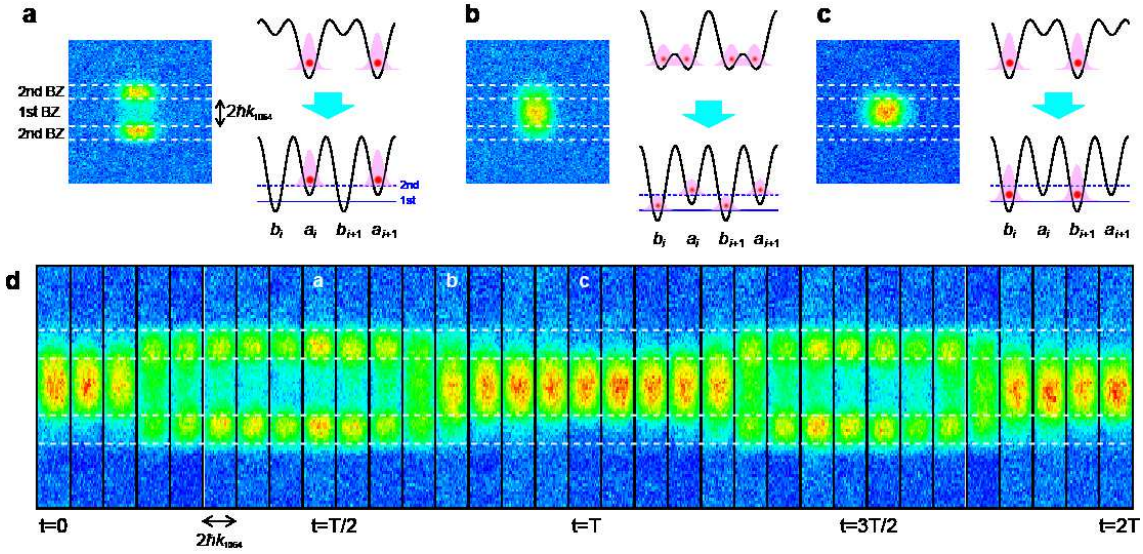

FIG. S 5. **Confirming occupancy of the lowest band. a**. Sublattice mapping technique. If a wave function is localized at sublattice site a_i, the wave function is projected to the 2nd band of the mapping lattice and thus the occupation of the sublattice site a_i can be measured via band mapping technique as the occupation of the 2nd band. The left image in **a** is a band mapped absorption image taken after 10 ms time-of-flight (five-times averaged). **b**. If the wave function is delocalized over both a_i and b_i, the wave function is mapped to both 1st and 2nd bands. **c**. If a wave function is localized at sublattice site b_i, its occupation is mapped to the 1st Brillouin zone. **d** Sublattice mapping measurements (five times averaged). The horizontal scale of the TOF images are half of the TOF images in **a**-**c**.

lowest band are still in the lowest band after pumping sequences. This result suggests that atoms localized on the B-sublattice $\{b_i\}$ can tunnel in the double-wells and then localize on the A-sublattice $\{a_i\}$. The atoms are well described by the lowest-band Wannier functions of the superlattice. The result also suggests that the atoms are mainly localized at A-sublattice or B-sublattice in our deep-lattice cRM pumping sequence and that the tunnelling only occurs when the Berry curvature has finite value.

S4. DETAILS OF THE *IN SITU* IMAGING

In this section, we discuss the stability of our *in situ* imaging. To evaluate a CM shift of an atomic cloud in real space, we measure the CM position from the *in situ* absorption imaging with a CCD camera (iXon, Andor). The CM position is derived from the Gaussian fitting to the integrated one-dimensional data. In our imaging setup, one pumping cycle, namely the cloud shift of $d = 532$ nm corresponds to 0.228 pixel on the CCD. The typical cloud width (FWHM) in the pumping direction is 3.7(5) pixels, corresponding to $16(2)d$.

Note that the CM shift after one pumping cycle is less than one pixel. However, since the Gaussian fit uses many data points (typically more than 20 pixels) as one can see in Fig.2c of the main text, we can reduce the fit uncertainty (1σ confidence) down to $0.3d$ for each image in Fig. 2 of the main text. Thus the error bars in the CM measurements mainly come from fluctuations of the cloud position, probably due to the fluctuation of the initial atom loading. Although we cannot suppress this fluctuation, we can reduce the statistical error to be smaller than the fitting uncertainty by taking a lot of data. In Fig. S6, we show an example of such repeated measurements. The error bars in the region of $0 \leq t \leq T$

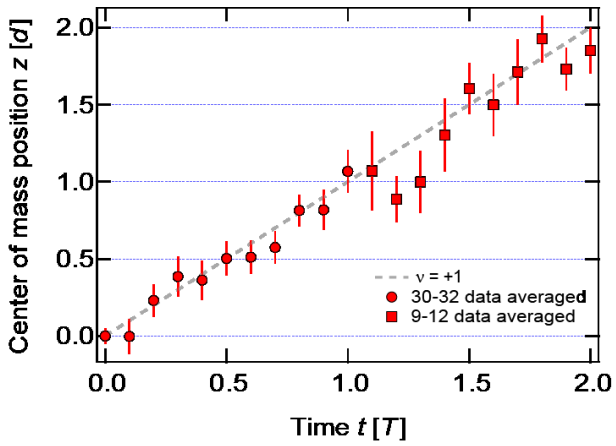

FIG. S 6. **Stability of *in situ* imaging.** The center of mass of the atomic cloud in the cRM pumping with depths of $(V_S, V_L) = (20, 26)E_R$. The error bars of the data in the region of $0 \leq t \leq T$ represent statistical errors of 30 to 32 independent measurements and those in region of $T < t \leq 2T$ are statistical errors of 9 to 12 independent measurements. The fitting uncertainty ($\sim 0.3d$) is not taken into account in these error bars.

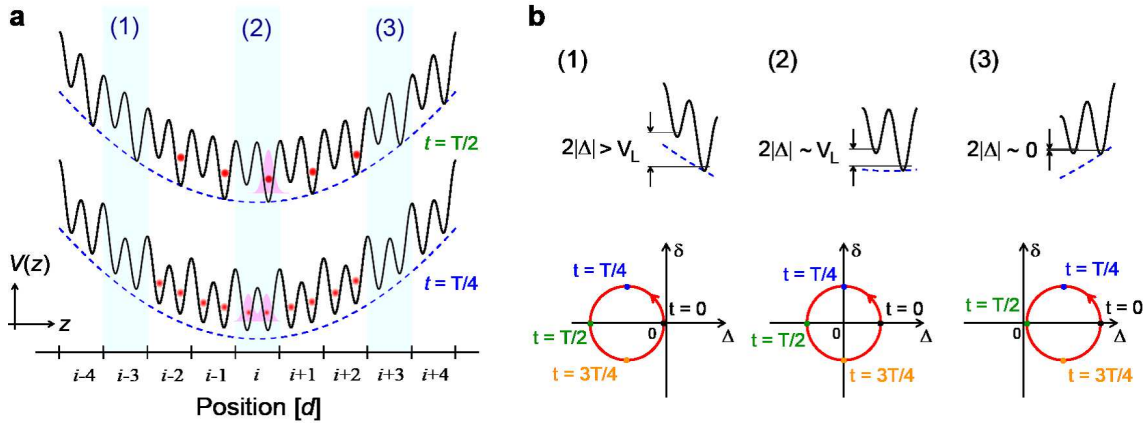

FIG. S 7. **Effect of the harmonic confinement. a** Schematics of the Rice-Mele superlattice in harmonic confinement. **b** The local lattice potentials in three different regions (1)-(3) are shown in the upper part. The lower figures of **b** are schematic trajectories of the Rice-Mele pump in these three regions.

represent statistical errors of 30 to 32 independent measurements and those in region of $T < t \leq 2T$ statistical errors of 9 to 12 independent measurements. One can clearly see that the amount of shift is quite close to an ideal pump ($\nu = 1$), indicated by a dashed line.

S5. EFFECT OF HARMONIC CONFINEMENT

In this section we discuss the effect of harmonic confinement on the pumping. As illustrated in Fig. S7a, our system is finite and not uniform due to the harmonic confinement. The spatial periodicity thus becomes worse as the CM of the cloud shifts away from the center of the trap. Moreover, since the local chemical potential also decreases as the CM of the cloud shifts from the center of the trap, the effective band gap becomes smaller and diabatic transition occurs more easily – the edge of the cloud is more "metallic". This can also be understood in the terms of the trajectory of the Rice-Mele pump as shown in Fig. S7b. The left (right) edge of the trajectory gets close to the degeneracy point as the cloud shifts to right (left), which suggest that the pumping should be saturated after a certain CM shift, depending on the strength of the confinement, while an ideal pumping is possible before the saturation. In Fig. 2 and also Fig. 4 of the main text, one can indeed see that the pumped amount starts to saturate after several cycles. S8 compares the behavior of the saturation for two different confinement strengths, which clearly shows that larger confinement induces an earlier onset of saturation.

This saturation point is also related to the value of the band gap. We actually observed that the saturation point becomes lower as we tune the long lattice depth V_L shallower corresponding to smaller minimum band gap. These observation suggests that the saturation point is determined by the competition between the band gap and the harmonic confinement. In other word, we can conclude that the atomic cloud are robustly pumped as long as the pumping system are protected by the gap.

[1] Thouless, D. J. Quantization of particle transport. *Phys. Rev. B* **27**, 6083–6087 (1983).

[2] King-Smith, R. D. & Vanderbilt, D. Theory of polarization of crystalline solids. *Phys. Rev. B* **47**, 1651–1654 (1993).

[3] Zak, J. Berry's phase for energy bands in solids. *Phys. Rev. Lett.* **62**, 2747–2750 (1989).

[4] Thouless, D. J., Kohmoto, M., Nightingale, M. P. & den Nijs, M. Quantized Hall conductance in a two-dimensional periodic potential. *Phys. Rev. Lett.* **49**, 405–408 (1982).

[5] Kitagawa, T., Berg, E., Rudner, M. & Demler, E. Topological characterization of periodically driven quantum systems. *Phys. Rev. B* **82**, 235114 (2010).

[6] Rice, M. J. & Mele, E. J. Elementary excitations of a linearly conjugated diatomic polymer. *Phys. Rev. Lett.* **49**, 1455–1459 (1982).

[7] Xiao, D., Chang, M.-C. & Niu, Q. Berry phase effects on electronic properties. *Rev. Mod. Phys* **82**, 1959–2007 (2010).

[8] Taie, S. *et al.* Matter-wave localization and delocalization of ultracold bosons in an optical Lieb lattice. Preprint at http://arXiv.org/abs/1506.00587 (2015).

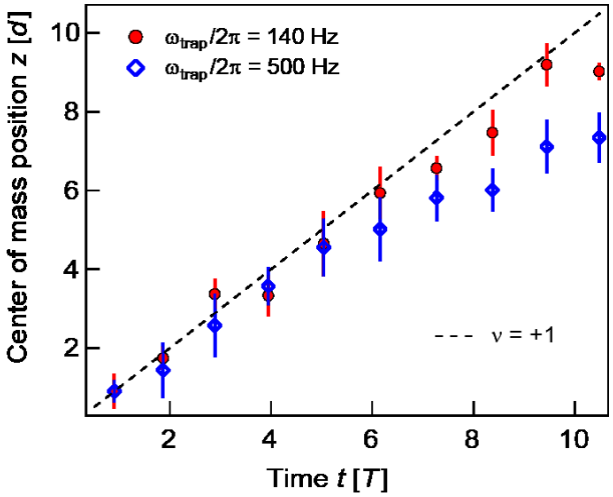

FIG. S 8. **Effect of the harmonic confinement in cRM pumping.** The cRM pumping with depths of $(V_S, V_L) = (20, 36)E_R$ at different confinement strengths. In the case of stronger confinement pumping ($\omega_{\mathrm{trap}}/2\pi \sim 500$ Hz, blue diamonds) starts to be saturated after a smaller number of cycles than that for the case of the weaker confinement ($\omega_{\mathrm{trap}}/2\pi \sim 140$ Hz, red circles).